EDGE ARTICLE

Check for updates

All publication charges for this article have been paid for by the Royal Society of Chemistry

Electrochemical CO$_2$ reduction catalyzed by atomically precise alkynyl-protected Au$_7$Ag$_8$, Ag$_9$Cu$_6$, and Au$_2$Ag$_8$Cu$_5$ nanoclusters: probing the effect of multi-metal core on selectivity†

Xiaoshuang Ma,‡[a] Fang Sun,‡[b] Lubing Qin,[a] Yonggang Liu,[a] Xiongwu Kang, [iD][a] Likai Wang,[c] De-en Jiang, [iD][d] Qing Tang [iD] *[b] and Zhenghua Tang [iD] *[ae]

Doping metal nanoclusters (NCs) with another metal usually leads to superior catalytic performance toward CO$_2$ reduction reaction (CO$_2$RR), yet elucidating the metal core effect is still challenging. Herein, we report the systematic study of atomically precise alkynyl-protected Au$_7$Ag$_8$, Ag$_9$Cu$_6$, and Au$_2$Ag$_8$Cu$_5$ NCs toward CO$_2$RR. Au$_2$Ag$_8$Cu$_5$ prepared by a site-specific metal exchange approach from Ag$_9$Cu$_6$ is the first case of trimetallic superatom with full-alkynyl protection. The three M$_{15}$ clusters exhibited drastically different CO$_2$RR performance. Specifically, Au$_7$Ag$_8$ demonstrated high selectivity for CO formation in a wide voltage range (98.1% faradaic efficiency, FE, at −0.49 V and 89.0% FE at −1.20 V *vs.* RHE), while formation of formate becomes significant for Ag$_9$Cu$_6$ and Au$_2$Ag$_8$Cu$_5$ at more negative potentials. DFT calculations demonstrated that the exposed, undercoordinated metal atoms are the active sites and the hydride transfer as well as HCOO* stabilization on the Cu–Ag site plays a critical role in the formate formation. Our work shows that, tuning the metal centers of the ultrasmall metal NCs *via* metal exchange is very useful to probe the structure–selectivity relationships for CO$_2$RR.

Introduction

The electrochemical CO$_2$ reduction reaction (CO$_2$RR) has been attracting increasing research efforts continuously, as it can convert CO$_2$ into valuable fuels and balance the carbon cycle.[1–4] So far, various metals including Au, Ag, Cu, *etc.* as catalytic materials have been investigated for CO$_2$RR.[5,6] Bimetallic or trimetallic catalysts usually exhibit superior catalytic

[a]New Energy Research Institute, Guangdong Provincial Key Laboratory of Atmospheric Environment and Pollution Control, School of Environment and Energy, South China University of Technology, Guangzhou Higher Education Mega Centre, Guangdong, 510006, China. E-mail: zhht@scut.edu.cn

[b]School of Chemistry and Chemical Engineering, Chongqing Key Laboratory of Theoretical and Computational Chemistry, Chongqing University, Chongqing, 401331, China. E-mail: qingtang@cqu.edu.cn

[c]School of Chemistry and Chemical Engineering, Shandong University of Technology, Shandong, 255049, China

[d]Department of Chemistry, University of California, Riverside, CA, 92521, USA

[e]Guangdong Provincial Key Laboratory of Functional Supramolecular Coordination Materials and Applications, Jinan University, Guangdong, 510632, China

† Electronic supplementary information (ESI) available: synthesis, characterization, supporting figures and tables. Details and crystal data of [Au$_2$Ag$_8$Cu$_5$(C≡C-^{t}Bu)$_{12}$]SbF$_6$ (CIF). CCDC 2072663. The videos for the metal exchange process to synthesize Au$_2$Ag$_8$Cu$_5$ from Ag$_9$Cu$_6$. For ESI and crystallographic data in CIF or other electronic format see https://doi.org/10.1039/d2sc02886g

‡ X. Ma and F. Sun contributed equally to this work.

performance than their homometallic counterparts due to the catalytic synergistic effects.[7,8] To improve the catalytic efficiency and advance the fundamental mechanistic understanding, one of the major challenges is the polydispersity of the catalyst. Specifically, despite the size, morphology, composition, even the coordination environment seems to be uniform in bulk or at a large-scale dimension, it can't offer a homogeneous chemical environment at the atomic level, making it extremely challenging to profoundly elucidate the mechanism and establish the structure–function relationship.

The emergence of atomically precise coinage metal nanoclusters (NCs) offers great opportunities to resolve the above problem due to their definitive size, morphology, composition, and more importantly, the crystallographically resolved structure can provide well-defined chemical environment to correlate the structure–performance relationship.[9–16] Pioneering work has been extensively conducted on thiolate-protected bimetallic NCs. For instance, in an early study, Jin group discovered that, compared to homogold Au$_{25}$ NC, monopalladium-doped Pd$_1$Au$_{24}$ NC can drastically inhibit the H$_2$ evolution, and had much higher CO product selectivity (faradaic efficiency for CO, FE$_{CO}$ = ~100%) at high potentials.[17] Zhuang *et al.* found that, compared with the parent Au$_{44}$ NC, Au$_{47}$Cd$_2$(TBBT)$_{31}$ (TBBT: 4-*tert*-butylbenzenelthiol) NC exhibited not only higher selectivity for CO (FE$_{CO}$ up to 96% at −0.57 V), but also a higher CO partial current density (j_{CO} = −3.67 mA

cm^{-2}) with a stronger suppression of the hydrogen evolution reaction (HER) (FE_{H2} = ~3.8%).[18] In another study, by only substituting four surface Au atoms in $Au_{23}(SR)_{16}$ with two Cd atoms, $Au_{19}Cd_2(SR)_{16}$ was prepared by Li *et al.*, and such modification greatly enhanced the selectivity of CO in CO_2RR (FE_{CO} = ~90 to 95% at −0.5 to −0.9 V), which is doubled compared to the undoped Au_{23} NC.[19] Recently, Sun *et al.* devised a strategy to control the cleavage of Au–S or S–C bonds by introducing Cd atoms, and identified the reaction sites of $Au_{25}(SR)_{18}$, $Au_{24}Cd_1(SR)_{18}$, $Au_{19}Cd_4(SR)_{18}$, and $Au_{38}Cd_4(SR)_{30}$ for CO_2RR.[20] In the above cases, DFT calculations disclosed that, the Cd doping altered the surface geometry and electronic structure of the NCs, which further changed the intermediate binding energy.

Noteworthily, for Au-based NCs, CO is the main product in CO_2RR test. Copper-based catalysts have demonstrated to be effective to convert CO_2 into highly valuable products including formate,[21] methanol,[22] methane,[23] and so on. Tang *et al.* synthesized a $Cu_{32}H_{20}L_{12}$ (L: a dithiophosphate ligand) NC, which can offer a unique selectivity of formate ($FE_{formate}$ = 90%) for CO_2RR at low overpotentials.[24] DFT calculations revealed that, the presence of the negatively charged hydrides in the NC played a critical role in determining the selectivity of the product, while the formate formation proceeded *via* the lattice-hydride mechanism.[24] Thanks to the versatile metal–ligand bonding moieties,[25–27] alkynyl ligands have been attracting more and more attentions to prepare coinage metal NCs in the past decade,[25,28,29] and homoleptic alkynyl-protected coinage metal NCs possess unique physicochemical properties and have found broad applications in semiconductor,[30] hypergolic fuels,[31] and biomedical regime.[32] Until so far, significant progress has been made on structure determination and formation mechanism study,[25,28] yet the cases on alkynyl-protected metal NCs for CO_2RR are still quite rare. Recently, our group reported the quite small all-alkynyl-protected $[Ag_{15}(C\equiv C\text{-}^tBu)_{12}]^+$ NC, which was able to convert CO_2 into CO with a FE_{CO} of ~95% at −0.6 V.[33] Also, the first case on homoleptic alkynyl-protected AgCu superatom of $[Ag_9Cu_6(C\equiv C\text{-}^tBu)_{12}]^+$ was prepared to compare the physicochemical properties with $[Au_7Ag_8(C\equiv C\text{-}^tBu)_{12}]^+$, and the two M_{15} clusters exhibited distinctly different optical properties due to the metal core difference.[34] The following questions arise immediately: will these two clusters have different CO_2RR performance as well? Furthermore, as both clusters are belonging to the M_{15} series, if the metal core is atomically tailored, how does the CO_2RR performance change? In another word, can we atomically tailor the core to probe the metal core effect of the M_{15} series toward CO_2RR? The above questions form the primary aim and goal of our current study.

Herein, we report the CO_2RR performance and comprehensive mechanistic study of atomically precise alkynyl-protected $[Au_7Ag_8(C\equiv C\text{-}^tBu)_{12}]SbF_6$ (Au_7Ag_8 in short hereafter), $[Ag_9Cu_6(C\equiv C\text{-}^tBu)_{12}]SbF_6$ (Ag_9Cu_6 in short hereafter), and $[Au_2Ag_8Cu_5(C\equiv C\text{-}^tBu)_{12}]SbF_6$ ($Au_2Ag_8Cu_5$ in short hereafter) NCs. As a note, in a recent study, Kang *et al.* reported a shortening of the A3-coupling reaction time from hours to minutes at higher temperatures (175 °C) catalyzed by a thermally robust,

trimetallic $Au_1Ag_{16}Cu_{12}(SSR)_{12}(PPh_3)_4$ NC (SSR: benzene-1,3-dithiolate), demonstrating the unique potential of trimetallic alloying in catalytic enhancement.[35] By using a chiral reducing agent, Hakkinen and Zheng groups reported a novel phosphine and thiolate ligand co-protected trimetallic $[Au_7Ag_6Cu_2(R\text{- or }S\text{-}BINAP)_3(SCH_2Ph)_6]SbF_6$ (BINAP: 2,2′-bis(diphenylphosphino)-1,1′-binaphthyl) NC with tertiary chiral nanostructure.[36] In this study, $Au_2Ag_8Cu_5$ is the first case of all-alkynyl-protected tri-metallic superatom documented so far. It can be synthesized by a metal exchange approach from Ag_9Cu_6, and X-ray crystallography reveals a body-centered-cubic (BCC) structure with an $Au@AuAg_4Cu_3@Ag_4Cu_2$ core configuration. Interestingly, the three M_{15}^+ NCs exhibited significantly different CO_2RR properties. Au_7Ag_8 can convert CO_2 into CO exclusively with FE_{CO} reaching 98.1% at −0.49 V, while CO and formate are the main products for Ag_9Cu_6 and $Au_2Ag_8Cu_5$ at more negative potentials, in which the highest $FE_{formate}$ value is 47.0% at −1.19 V and 28.3% at −0.99 V, respectively. In addition, Ag_9Cu_6 and Au_7Ag_8 can inhibit H_2 evolution effectively with FE_{H2} less than 10% in the whole tested potential range. Density functional theory (DFT) calculations disclosed that –C≡CR removal from the intact NC can expose the undercoordinated metal atom as the catalytic site to significantly promote the activity and selectivity of CO_2RR. In particular, the formation of negative hydride is the key for the exclusive formate formation on Ag_9Cu_6 and $Au_2Ag_8Cu_5$.

Results and discussion

Preparation and characterization of Au_7Ag_8, Ag_9Cu_6, and $Au_2Ag_8Cu_5$ NCs

Au_7Ag_8 and Ag_9Cu_6 NCs were first synthesized by following the method in our previous report, in which the crystal structure and optical properties of the two NCs were compared.[34] Note that, the fabrication and total structure of Au_7Ag_8 NC was first reported by Wang *et al.* in 2016,[37] and our anti-galvanic synthetic approach can improve the yield drastically.[34] In this study, $Au_2Ag_8Cu_5$ NC was synthesized by a site-specific metal exchange method by a reaction between $Me_2SAu(I)Cl$ and Ag_9Cu_6 NC with a controlled stoichiometric ratio. The detailed synthetic procedure can be found in ESI,† and the relevant elucidation of the process will be discussed next.

Subsequently, the chemical composition of the three NCs were verified by electrospray ionization mass spectrometry (ESI-MS). As illustrated in Fig. 1a, the sharp peak at m/z = 3214.8510 and 2325.5677 is assigned to Au_7Ag_8 and Ag_9Cu_6, respectively, and the well-matched experimental/simulated isotopic pattern (Fig. S1a and b†) confirmed the molecular composition of Au_7Ag_8 and Ag_9Cu_6. In addition, the main peak at m/z = 2548.6640 corresponds well with $[Au_2Ag_8Cu_5(C_6H_9)_{12}]^+$ (cal.: 2548.6634 Da, deviation: 0.0006 Da), and the isotopic patterns of the NC match perfectly with the simulated results (Fig. S1c†). There is also the one Au atom exchanged product of $AuAg_8Cu_6$ NC (indicated by ▲, see enlarged spectra in Fig. S1f†), and the fragments of Au_7Ag_8 and Ag_9Cu_6 NCs are identified in Fig. S1d and e,† respectively. To further confirm the metallic ratio in $Au_2Ag_8Cu_5$, X-ray photoelectron spectroscopy (XPS, Fig. S2†)
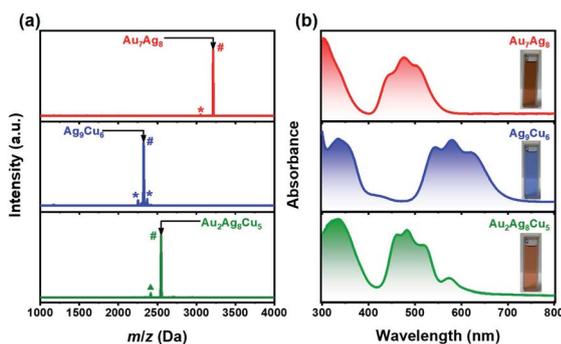
Fig. 1 (a) Positive-mode ESI-MS and (b) absorbance spectra of Au_7Ag_8, Ag_9Cu_6, and $Au_2Ag_8Cu_5$ NCs. The asterisk (*) and octothorpe (#) indicate the fragment ion and molecular ion of Au_7Ag_8, Ag_9Cu_6, and $Au_2Ag_8Cu_5$ NCs, respectively, and the triangle (▲) indicates the $AuAg_8Cu_6$ NC product in the $Au_2Ag_8Cu_5$ sample.

and energy-dispersive X-ray spectroscopy (EDS, Fig. S3†) were conducted. The atomic ratio of Au/Ag/Cu is 1.9/8.1/5.3 (2.0/8.7/5.7) and 1.5/6.7/4.2 (2.0/8.9/5.5) from XPS (Table S1†) and EDS (Fig. S3†), respectively, both are in agreement with the theoretical value (2/8/5). The XPS survey scan spectra confirmed the presence of the essential elements (Fig. S2a†). The binding energy of the Au $4f_{7/2}$ electrons is located at 84.43 eV, between bulk Au (84.0 eV)[38] and Au(I) (84.5 to 86.0 eV)[38] (Fig. S2b†). Furthermore, the binding energy of the Ag $3d_{5/2}$ electrons is located at 368.65 eV (Fig. S2c†), indicating that the valence state of Ag atoms in $Au_2Ag_8Cu_5$ is +1.[39] In addition, the binding energy of Cu $2p_{3/2}$ (933.40 eV) agrees well with that of Cu(I) (933.3 eV),[40] implying that Cu atoms are present as Cu(I) (Fig. S2d†). Moreover, as illustrated in Fig. 1b, the fingerprint absorbance peaks of $Au_2Ag_8Cu_5$ NC are located at 335, 461, 484, 521, and 571 nm, quite different from that of Au_7Ag_8 (313, 339, 422, 477, and 506 nm) and Ag_9Cu_6 (333, 357, 422, 544, 579, and 620 nm) NCs. Nevertheless, we monitored the absorbance change in the formation process of $Au_2Ag_8Cu_5$. As shown in Fig. S4a,† the absorbance feature of Ag_9Cu_6 NC disappeared immediately upon the addition of $Me_2SAu(I)Cl$, while a new absorption band at ∼484 nm arose. There is an obvious colour change at the timing point of $Me_2SAu(I)Cl$ addition (Fig. S4b†). In 1 h, the characteristic peak at 484 nm from $Au_2Ag_8Cu_5$ gradually arose, meanwhile the absorbance peak at 571 nm can be identified. The metal exchange process occurs very fast, and as manifested by the two visualized video records (see Video 1† under room light and Video 2† under 365 nm UV-light as additional ESI†). In addition, we also studied the photoluminescence property of the $Au_2Ag_8Cu_5$ NC. As shown in Fig. S5,† $Au_2Ag_8Cu_5$ NC strongly emits in the near-infrared region (λ_{max} = 825 nm), which is much stronger than that of Au_7Ag_8 NC, while Ag_9Cu_6 NC is not photoluminescent.[34] Given the standard absorbance curve (Fig. S6a†) of $Au_2Ag_8Cu_5$ NC, according to Lambert–Beer's law, the molecular absorptivity (ε) of $Au_2Ag_8Cu_5$ NC can be determined ($\varepsilon = 1.88 \times 10^4 \text{ M}^{-1} \text{ cm}^{-1}$), as summarized in Table S2.† Subsequently, the yield of $Au_2Ag_8Cu_5$ NC was calculated as ∼66.85% (based on Cu). The details of the calculation process can be found in ESI† (Fig. S6b and Table S3†).

Elucidating metal exchange process from Ag_9Cu_6 to $Au_2Ag_8Cu_5$

Tailoring the metal core while retaining the other parts has been proven as an effective approach to modify the physicochemical property and enhance the functionality of thiolate-protected metal NCs.[41] Such metal core tailoring is actually part of the tailoring chemistry of metal nanoclusters.[42] To the best of our knowledge, no case on metal core tailoring has been reported for homoleptic alkynyl-protected coinage metal NCs. Inspired by the findings in thiolate-protected metal NCs, herein, $Au_2Ag_8Cu_5$ was synthesized by a controlled stoichiometry of $Me_2SAu(I)Cl$-to-Ag_9Cu_6 (=2) through atomic-level tailoring by metal exchange (Fig. 2a). The total structure comparison between $Au_2Ag_8Cu_5$, Ag_9Cu_6, and Au_7Ag_8 will be discussed in the next session, nevertheless, the detailed five-step transformation from Ag_9Cu_6 to $Au_2Ag_8Cu_5$ is presented in Fig. 2b, and the corresponding chemical reaction equations are shown in Fig. 2c.

Firstly, 1 eq. of $Me_2SAu(I)Cl$ was added to react with Ag_9Cu_6, and one Au(I) atom replaces one Ag(I) atom to form a $Ag@Ag_7$-$Au@Cu_6$ kernel (Step I). It is a metathesis reaction, and Me_2-$SAg(I)Cl$ is also generated in the solution. Note that, the driving force of such heteroatom exchange is probably the interaction between the Cl⁻ ion and the Ag(I) atoms on the Ag_8 cube. Subsequently, the as-formed intermediate was transformed into more stable molecule (kernel: $Au@Ag_8@Cu_6$) *via* galvanic reaction, in which the Au(I) atom is reduced by the central Ag(0) atom (determined by DFT structures with Mulliken charges in Table S4†),[34] and the two atoms exchanged the position with each other (Step II). As a note, such Au heteroatom diffusion phenomenon has been previously documented in thiolate-protected alloy NCs,[43,44] for instance, Xie and coworkers discovered that, the Au heteroatom diffuses into the surface layer of the Ag_{13} icosahedron kernel and finally is reduced by the central Ag(0) atom, forming thermodynamically stable $AuAg_{24}(MHA)_{18}$ molecule.[45] Then, in the presence of another 1 eq. of $Me_2SAu(I)Cl$, like the first step, $Au_2Ag_7Cu_6$ (kernel: $Au@Ag_7Au@Cu_6$) NC was formed by the metal exchange reaction (Step III). Consequently, the Cu atoms around the Au atom in the M_8 cube are activated and can react with $Me_2SAg(I)Cl$ generated in the previous steps, and one Ag(I) atom exchanges with one Cu(I) atom in the Cu_6 octahedron (Step IV). Finally, three Ag(I) atoms on the M_8 cube were exchanged by three Cu(I) atoms to form $Au_2Ag_8Cu_5$ NC with the optimal thermodynamic stability (Step V).

It is worth pointing out that, the precise stoichiometric ratio of $Me_2SAu(I)Cl$-to-Ag_9Cu_6 (=2) is critical for yielding the optimal amount of $Au_2Ag_8Cu_5$ NC. In fact, different ratios of $Me_2SAu(I)Cl$ (0.4 eq., 1.0 eq., 1.6 eq., 2.0 eq., and 2.4 eq. per Ag_9Cu_6) were tested, and the results are shown in Fig. S7.† As depicted in the absorbance change in Fig. S7a,† with the increasing of the $Me_2SAu(I)Cl$ amount (from 0.4 to 2.0 eq.), the intensity of the characterstic peak (at 579 nm) from Ag_9Cu_6 decreased gradually (totally disappeared with 2 eq.), while the characteristic peak (at 484 nm) from $Au_2Ag_8Cu_5$ gradually became intensified. However, when it increased to 2.4 eq., the intensity of the peak

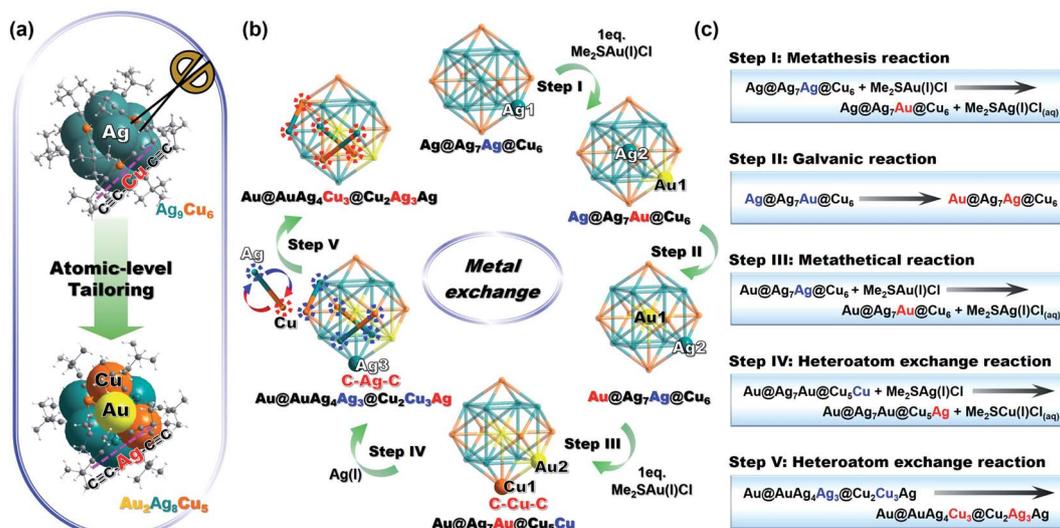**Fig. 2** (a) Synthesis of the [Au$_2$Ag$_8$Cu$_5$(C≡C-^{t}Bu)$_{12}$]$^+$ NC by atomic-level tailoring. (b) Metal exchange process from Ag$_9$Cu$_6$ NC to Au$_2$Ag$_8$Cu$_5$ NC *via* a five-step process. Color legend: Au, yellow; Ag, cyan; Cu, orange; C, gray, H, white. (c) Equations of the Au$_2$Ag$_8$Cu$_5$ formation by metal exchange from Ag$_9$Cu$_6$ NC. The atoms before (blue) and after (red) the reaction.

at 484 nm slightly decreased. Such trend can be more clearly observed in Fig. S7b and c,† that is, with lower amounts of Me$_2$SAu(I)Cl (0.4 to 1.6 eq.), Ag$_9$Cu$_6$ NC is not fully converted, and with extra amount of Me$_2$SAu(I)Cl, Ag$_9$Cu$_6$ can be fully converted but polydispersed mixture was obtained. For instance, in the presence of 8 eq. Me$_2$SAuCl, a series of [Au$_x$-Ag$_8$Cu$_{7-x}$ (C≡C-^{t}Bu)$_{12}$]$^+$ (x = 1 to 7) molecules including Au$_2$-Ag$_8$Cu$_5$ and Au$_7$Ag$_8$ NCs were acquired, as confirmed by the ESI-MS spectra in Fig. S8.† Unfortunately, several attempts were conducted to separate the intermediate but was not successful, mainly due to that, this reaction occurs too fast (the whole process is finished in 1 h). We also noticed that, in the previous report, Wang *et al.* employed Cu atoms to react with Au$_7$Ag$_8$ clusters, and a series of cluster mixture [Cu$_n$Ag$_8$Au$_{7-n}$ (C≡C-^{t}Bu)$_{12}$]$^+$ (n = 0 to 6) including Au$_2$Ag$_8$Cu$_5$ NC (n = 5) was identified by mass spectrometry but the separation was also not performed neither.[37] Therefore, the exact stoichiometric ratio of 2 is the optimal value and also very critical.

Structural comparison of the three M$_{15}$ NCs

Subsequently, the atomic packing structure of Au$_2$Ag$_8$Cu$_5$ was examined by single crystal X-ray diffractometer (SC-XRD). As illustrated in Fig. S9,† Au$_2$Ag$_8$Cu$_5$ crystallizes in space group of $R\bar{3}$, and each unit cell has a SbF$_6^-$ counterion, indicating that Au$_2$Ag$_8$Cu$_5$ NC possesses a +1 charge. The detailed structural parameters are summarized in Table S5.† The overall structure of monocationic Au$_2$Ag$_8$Cu$_5$ is shown in Fig. 3a, which contains two Au atoms, eight Ag atoms, five Cu atoms, and twelve *tert*-butylacetylene ligands, hence the molecule can be formulated as [Au$_2$Ag$_8$Cu$_5$(C≡C-^{t}Bu)$_{12}$]SbF$_6$. As illustrated in the space-filling structure, one Au site, five Cu sites, and eight Ag sites on the surface of Au$_2$Ag$_8$Cu$_5$ are exposed partially, which might result in the differences in catalytic performance compared with the other M$_{15}$ NCs (Ag$_9$Cu$_6$ and Au$_7$Ag$_8$). As a note, all the

currently reported alkynyl-protected M$_{15}$ NCs such as Ag$_9$Cu$_6$, Au$_7$Ag$_8$, and Ag$_{15}$ have only one type of ^{t}Bu-C≡C-M-C≡C-^{t}Bu (M = Cu/Au/Ag) linear motif.[33,34] However, for Au$_2$Ag$_8$Cu$_5$, there are five types of ^{t}Bu-C≡C-M-C≡C-^{t}Bu (M = Cu/Ag) motifs on the surface, in which the coordination mode of ^{t}Bu-C≡C– ligands are μ$_2$-η$_1$ (Ag/Cu), η$_1$ (Ag1/Ag2) for motif 1; μ$_2$-η$_1$ (Au/Ag/Cu), η$_1$ (Ag3) for motif 2; μ$_2$-η$_1$ (Au/Ag/Cu), η$_1$ (Ag4) for motif 3; μ$_2$-η$_1$ (Au/Ag/Cu), η$_1$ (Cu1) for motif 4 and μ$_2$-η$_1$ (Au/Ag), η$_1$ (Cu2) for motif 5, respectively (Fig. 3b). As a result, the σ (Cu2–C) and π (Ag/Cu–C) bond lengths of motif 5 (average value: 1.870 Å and 2.389 Å) are shorter than those of motifs 1, 2, 3, and 4 (average value: 1.894 Å and 2.392 Å; 1.893 Å and 2.395 Å; 1.894 Å and 2.398 Å; and 1.873 Å and 2.394 Å, Table S6†). Motif 5 in Au$_2$-Ag$_8$Cu$_5$ is nearly identical with the motif in Ag$_9$Cu$_6$. The average σ and π bond lengths of motifs on the surface of Au$_2$Ag$_8$Cu$_5$ (average 1.886 Å and 2.394 Å) are longer than those of Ag$_9$Cu$_6$ (average 1.870 Å and 2.381 Å) and shorter than those of Au$_7$Ag$_8$ (average 1.982 Å and 2.513 Å) (Table S7†). Note that, such different types of motifs can lead to the distortion of the kernel structure of Au$_2$Ag$_8$Cu$_5$. Furthermore, Au$_2$Ag$_8$Cu$_5$ adopts structural feature from both Au$_7$Ag$_8$ and Ag$_9$Cu$_6$, as it has the same central Au atom with Au$_7$Ag$_8$ and a more similar outlayer (Ag$_4$Cu$_2$ *vs.* Cu$_6$) with Ag$_9$Cu$_6$ (Fig. 3c). Specifically, the anatomical structure of Au$_2$Ag$_8$Cu$_5$ is compared with the two bimetallic NCs. As shown in Fig. 3d, Au$_2$Ag$_8$Cu$_5$ adopts a core–shell–shell configuration (M$_{core}$@M$_{cube}$@M$_{octahedron}$) of Au@AuAg$_4$Cu$_3$@Ag$_4$Cu$_2$, similar to the other two NCs, but there are some difference in the M$_{cube}$ and M$_{octahedron}$ layers. For Au$_2$Ag$_8$Cu$_5$, the two layers consist of the heteroatoms (AuAg$_4$Cu$_3$ and Cu$_2$Ag$_4$), while there are the homoatoms in the middle layer (Ag$_8$) and outer layer (Au$_6$ and Cu$_6$) of Au$_7$Ag$_8$ and Ag$_9$Cu$_6$. Such structural difference leads to the difference in average bond lengths spread on different layers of the three NCs (Table S8†). Compared with Au$_7$Ag$_8$ and Ag$_9$Cu$_6$, the doped Au and Cu
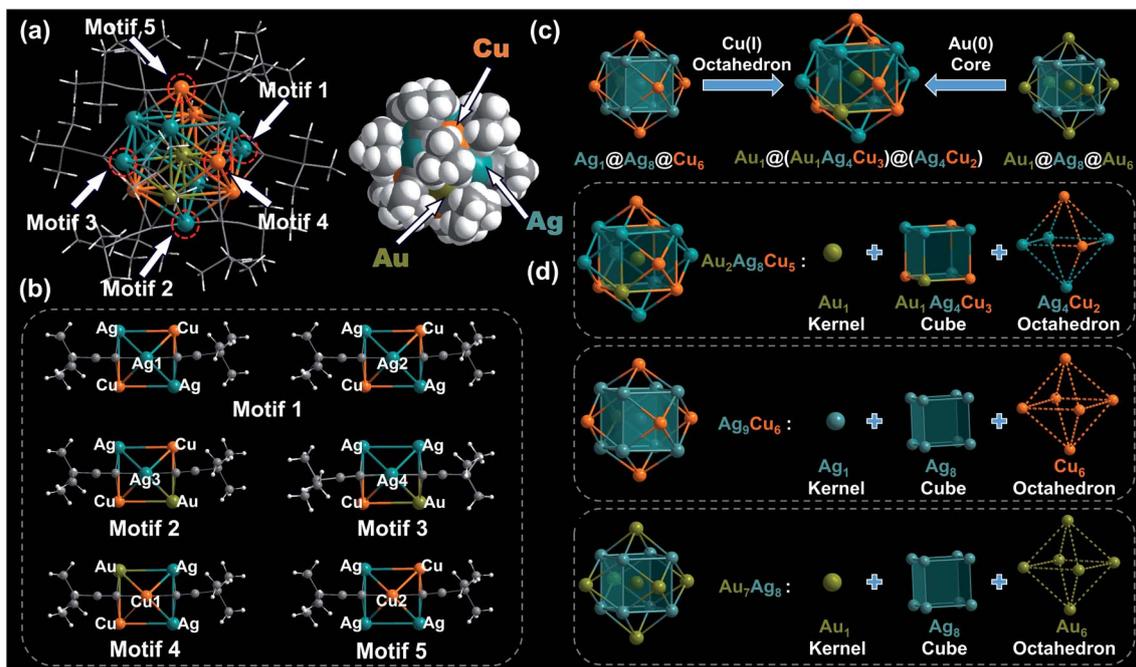
Fig. 3 Structural analysis in body-centered cubic (BCC) M_{15} NCs. (a) Overall and space-filling structure of monocationic $Au_2Ag_8Cu_5$, (b) the five types of linear $^tBu-C\equiv C-CuC\equiv C-^tBu$ staple motifs on the metal surface. Coordination modes of $^tBu-C\equiv C$ ligands: $\mu_2-\eta_1$ (Ag/Cu), η_1 (Ag); $\mu_2-\eta_1$ (Au/Ag/Cu), η_1 (Ag); $\mu_2-\eta_1$ (Au/Ag/Cu), η_1 (Cu) and $\mu_2-\eta_1$ (Ag/Cu), η_1 (Cu). (c) Structural analysis and (d) anatomy of BCC M_{15} kernel in $Au_2Ag_8Cu_5$, Ag_9Cu_6, and Au_7Ag_8, respectively. Color legend: Au, yellow; Ag, cyan; Cu, orange; C, gray; H, white.

heteroatoms lead to the M_{cube} in $Au_2Ag_8Cu_5$ slightly relaxed, as the average adjacent M_{cube}–M_{cube} bond (3.414 Å) length is larger than those in the other two NCs (3.333 Å and 3.283 Å). However, there are four Ag atoms in the $M_{octahedron}$ of $Au_2Ag_8Cu_5$, and the bonding lengths of the outer layer in $Au_2Ag_8Cu_5$ are slightly longer than those of Ag_9Cu_6 (e.g. $M_{octahedron}$–C_{ligand}: 1.886 Å vs. 1.870 Å; M_{cube}–C_{ligand}: 2.394 Å vs. 2.381 Å), further attesting the similarity of the outer layer between $Au_2Ag_8Cu_5$ and Ag_9Cu_6.

Electrocatalytic CO_2 reduction performance of the three M_{15} NCs in flow cell

As the three NCs possess a M_{15} configuration yet different metal core and significant discrepancies are observed on the physiochemical properties (e.g. optical absorbance), we wonder whether they have different catalytic properties. To probe the metal core effect, we next examined the electrocatalytic performance of the three catalysts on gas diffusion electrode (GDL, 2 × 1.5 cm²) toward CO_2RR by constant-potential electrolysis (CPE) measurements at various applied potentials in a custom-designed flowcell (Fig. 4a) (the electrochemical measurement details can be found in ESI†). The linear scanning voltammetry (LSV) was first conducted for Au_7Ag_8/GDL, Ag_9Cu_6/GDL, and $Au_2Ag_8Cu_5$/GDL. As depicted in Fig. S10,† for all the samples, a sudden decrease in the reduction current can be observed after the first potential sweep (black line) along with the onset potential shifted positively. In the second and third sweeps (red and blue line), the resulting current and onset potential remained unchanged. It suggests that, all the catalysts were activated, and such ligand stripping phenomenon has been

recorded in thiolate-protected Au_{25} NCs in the CO_2 electroreduction process as well.[46]

For all the catalysts, CO is the main product at more positive potentials, and formate at more negative potentials was also detected in the liquid phase by ^1H-NMR for the two Cu-containing catalysts (Fig. S11 and S12†). As shown in Fig. 4b, Au_7Ag_8 exhibited high selectivity for CO formation, evidenced by the higher FE_{CO} values at all tested potentials, ranging from ~86.6% at −0.39 V to ~98.1% at −1.19 V (vs. RHE). In contrast, for both Ag_9Cu_6 and $Au_2Ag_8Cu_5$, a similar volcanic shape on the FE_{CO} value is observed, in which the highest FE_{CO} value of ~94.2% and ~95.0% at −0.49 V is obtained for Ag_9Cu_6 and $Au_2Ag_8Cu_5$, respectively. However, for these two NCs, CO has higher FEs at more positive potentials, whereas the FE for formate ($FE_{formate}$) increases rapidly when the potential goes more negatively (Fig. 4c). The largest $FE_{formate}$ value for Ag_9Cu_6 and $Au_2Ag_8Cu_5$ is 47.0% at −1.19 V and 28.3% at −0.99 V, respectively. However, the $FE_{formate}$ value for $Au_2Ag_8Cu_5$ decreased to less than 20% at −1.19 V. Impressively, for both bimetallic NCs of Ag_9Cu_6 and Au_7Ag_8, the H_2 evolution can be significantly suppressed, as the FE_{H_2} is less than 10% in the whole tested potential range (Fig. S13a†). However, for $Au_2Ag_8Cu_5$, when the potential goes more negatively, the HER becomes more dominant, and the highest FE_{H_2} can reach 37.0% at −1.19 V. The total FE values of the products for the three catalysts were presented as a function of applied potential from −0.59 V to −1.19 V, showing that CO, H_2, and formate are the main products with a total FE value close to 100% in the whole potential range (Fig. 4d). No other product was detected
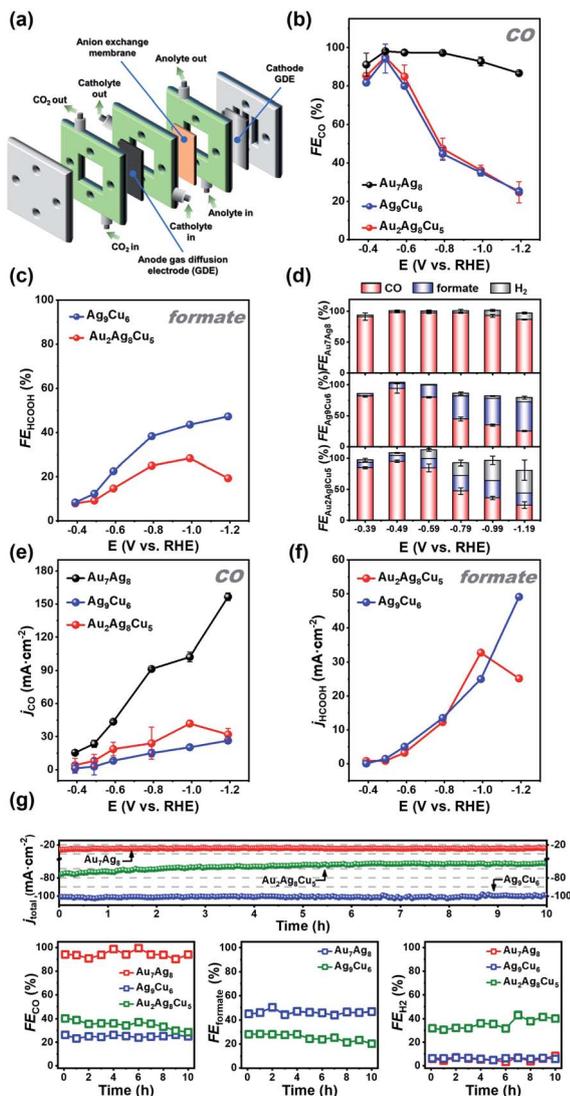
Fig. 4 (a) Exploded diagrams of the electrochemical reactors for CO_2 electroreduction in flow cell. (b) CO and (c) formate faradaic efficiency for Au_7Ag_8, Ag_9Cu_6, and $Au_2Ag_8Cu_5$ NC/GDLs examined at different applied potentials. (d) FEs for various CO_2RR products obtained on the three NC/GDLs. The corresponding (e) CO and (f) formate partial current density. (g) Long-term stability of Au_7Ag_8/GDL, Ag_9Cu_6/GDL, and $Au_2Ag_8Cu_5$/GDL at −0.49 V, −1.19 V, and −0.99 V (vs. RHE), respectively. (top) i−t curve; (bottom) FEs of CO, H_2, and formate at different time.

by NMR or GC. By deducting H_2, at −0.49 V, the highest FE_{CO} for Au_7Ag_8 is ∼98.1%, while the highest $FE_{CO+formate}$ for Ag_9Cu_6 and $Au_2Ag_8Cu_5$ is ∼100.0% and ∼97.4%, respectively, indicating the three NCs can efficiently convert CO_2 into value-added carbon products (Fig. 4d). Meanwhile, the CO partial current density (j_{CO}) increased with the increasing of applied potential for the Au_7Ag_8 and Ag_9Cu_6 catalysts, and j_{CO} reached the maximal value at −0.99 V then diminished at −1.19 V for $Au_2Ag_8Cu_5$ (Fig. 4e). Au_7Ag_8 had a much larger j_{CO} value than Ag_9Cu_6 and $Au_2Ag_8Cu_5$ at all potentials, further manifesting its unique advantage for converting CO_2 into CO exclusively. Furthermore, the partial current density of formate ($j_{formate}$) for Ag_9Cu_6 and $Au_2Ag_8Cu_5$

exhibited the same trend with the $FE_{formate}$ in the tested potential range (Fig. 4f), that is, $j_{formate}$ increased from −0.39 V to −1.19 V, reaching the maximal value of 49.1 mA cm^{-2} at −1.19 V for Ag_9Cu_6, however, for $Au_2Ag_8Cu_5$, it first increased then decreased, and the maximal value is 32.7 mA cm^{-2} at −0.99 V. This is mainly due to that the HER process became dominant at very high negative potentials (Fig. S13b†).

Stability is another important criterion to evaluate the catalytic property of the electrocatalyst, hence the long-term stability of Au_7Ag_8, Ag_9Cu_6, and $Au_2Ag_8Cu_5$ was tested at −0.49 V, −1.19 V, and −0.99 V, respectively. As illustrated in Fig. 4g, the current density and corresponding FE value of Au_7Ag_8 and Ag_9Cu_6 remained almost unchanged after 10 h's continuous operation, indicating robust long-term durability, however, under the same conditions, the current density of $Au_2Ag_8Cu_5$ decreased about 15% (from 75.4 to 64.1 mA cm^{-2}), meanwhile the $FE_{CO+formate}$ decreased and FE_{H_2} increased gradually, presumably due to that the asymmetric metal core of $Au_2Ag_8Cu_5$ is easier to decompose and/or aggregate during the electrocatalytic process. We conducted the MS measurement of the three NCs before and after CO_2RR to examine the change. As shown in Fig. S14,† for the Cu-containing NCs, the molecular ions with strong signal ($m/z = 2548.6640$ for $Au_2Ag_8Cu_5$, $m/z = 2325.5677$ for Ag_9Cu_6) are still dominant, indicating both clusters are rather robust. However, for both clusters, some peaks in the lower m/z region appeared, suggesting some of the cluster molecules decomposed. For $Au_2Ag_8Cu_5$, after CO_2RR, two peaks with $m/z = 1112.4193$ (Fragment A) and $m/z = 1471.6617$ (Fragment B) can be assigned to Au_4L_4 (L: C_6H_9, cal. MW: 1112.4183) and $Au_5L_6^+$ (cal. MW: 1471.6608), respectively. In addition, compared to product A, the peak intensity of Au_2-Ag_8Cu_5 decreased, suggesting that some $Au_2Ag_8Cu_5$ molecules might decompose to Au-alkynyl complexes and/or metal nanoparticles; for Ag_9Cu_6, after CO_2RR, there are three peaks appearing at $m/z = 1020.8771$ (Fragment A), 1099.9494 (Fragment B), and 1183.0180 (Fragment C), which can be assigned to $Ag_2Cu_5L_6^+$ (cal. MW: 1020.8762), $Ag_2Cu_5L_7^+$ (cal. MW: 1099.9485), and $Ag_2Cu_5L_8^+$ (cal. MW: 1183.0171), respectively. Also, there is one peak with m/z at 2476.3047 (D), which can be assigned to $Ag_{12}Cu_2L_{13}^+$ (cal. MW: 2476.3039), and it is probably formed in the chamber during the MS measurement. For Au_7Ag_8, after CO_2RR, there are two minor peaks appearing at $m/z = 3053.0904$ (Fragment A) and 2937.2619 (Fragment B), which can be assigned to $Au_7Ag_8L_{10}^+$ (cal. MW: 3053.0910) and $Au_6Ag_8L_{11}^+$ (cal. MW: 2937.2625), respectively. These results indicate that, the majority of the cluster molecules can be well preserved during the CO_2RR process.

Furthermore, we also tested the recover capability of the Ag_9Cu_6 and $Au_2Ag_8Cu_5$ catalysts for CO_2RR. Using the 579 and 484 nm fingerprint absorbance peak as the metric, the absorbance change can be quantified and employed to estimate the recovery rate (Fig. S15 and S16†). It is worth noting that, besides the intensity of the characteristic peak decreased with different extents at different potentials, the whole absorbance feature of these two NCs remained intact. The calculated results are summarized in Tables S9 and S10.† Specifically, from −0.39 V to −1.19 V, the intensity of the absorbance peak at 579 nm

decreased gradually, and the recovery rate of these two NCs decreased as well. Also, the recovery rate of Ag_9Cu_6 ranges from 30.4% to 96.6%, higher than that of $Au_2Ag_8Cu_5$ (21.0% to 89.7%) at all applied potentials, in good agreement with the finding in the i–t test.

The observation that all M_{15} NCs exhibited high catalytic selectivity of CO_2 electroreduction to CO at the low potentials and that the clusters containing Cu metals, namely Ag_9Cu_6 and $Au_2Ag_8Cu_5$, were found to generate formate products is interesting. We then compared the formation selectivity of formate and CO of the three M_{15} NCs with recently reported atomically precise metal nanoclusters in CO_2RR, as summarized in Table S11 and S12†, respectively. Although the reports were conducted in different cell type such as H-cell, flow-cell and MEA-cell, it can be noted that, the formate selectivity of the Ag_9Cu_6 and Au_2-Ag_8Cu_5 clusters is lower than the Cu_{32} cluster, but much higher than the Au_{25} cluster and all the AuCd alloy clusters. For CO formation selectivity, the highest FE_{CO} value of the Au_7Ag_8, Ag_9Cu_6, and $Au_2Ag_8Cu_5$ clusters are all over 94%, at least comparable with, if not superior to, the Au, Ag clusters and the AuCd, AuPd, AuAg alloy clusters. Particularly, the FE_{CO} value of the Au_7Ag_8 cluster can reach as high as 98.1%, larger than most of the recent reports, quite close to the $Au_{25}(PET)_{18}$ and Au_{24}-$Pd_1(PET)_{18}$ clusters (∼100% for both).

CO_2RR mechanistic study by DFT calculations

To deeply comprehend the electrocatalytic mechanism, we next performed DFT calculations (see ESI† for computational details) to determine the optimal catalytic site and analyze the selectivity difference. To simplify the calculation, all –C≡C-^{t}Bu ligands are replaced with –C≡C-CH_3. The optimized structure based on the crystal structure of $Au@AuAg_4Cu_3@Ag_4Cu_2$ is used as a model for DFT calculation, as shown in Fig. S17.† On the intact $[Au_7Ag_8(C≡C-CH_3)_{12}]^+$ (Fig. S18a†) and $[Ag_9Cu_6(C≡C-CH_3)_{12}]^+$ (Fig. S18b†), CO_2RR and HER compete on the same staple metal site (Au for $[Au_7Ag_8(C≡C-CH_3)_{12}]^+$ and Cu for $[Ag_9Cu_6(C≡C-CH_3)_{12}]^+$). While for $[Au_2Ag_8Cu_5(C≡C-CH_3)_{12}]^+$ NC, the staple Cu acts as the active site for HCOO* binding, while *COOH, *CO, and *H tend to bond with the sub-surface Au atom (Fig. S18c†). The free energy diagrams of CO_2RR and HER on these three intact systems are depicted in Fig. 5a, c, and e, and the H_2 pathway is thermodynamically more favourable than CO_2RR. In addition, we found that the bonding of *H on clusters containing copper is stronger. To uncover this phenomenon, we performed Bader charge analysis of metal active site (Table S13†), which intuitively shows that *H on Ag_9Cu_6 has the most negative charge (-0.29 |e|), indicating a stronger adsorption. However, *H has the strongest bonding on $Au_2Ag_8Cu_5$ cluster, which is possibly due to the special coordination environment of active Au atom, so that Au with greater electronegativity can rob electrons from the surrounding Ag or Cu. Therefore, the active Au here is negatively charged (-0.15 |e|) and interacts strongly with *H.

Inspired by related studies[17,19,46] and our recent finding on Ag_{15} NC for CO_2RR,[33] ligand removal to expose under-coordinated metal atom may serve as the electrocatalytic active
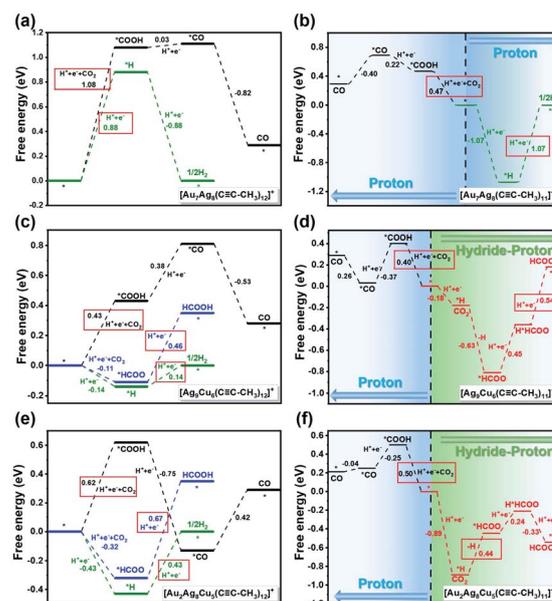

Fig. 5 (a, c and e) Comparison of CO_2RR vs. HER on three intact NCs. (b, d and f) Reaction scheme for CO_2 electroreduction on single ligand-removed clusters to form CO via the proton mechanism (blue region) and to form formate via the hydride–proton mechanism (green region) at zero applied potential. The reaction step with the highest free-energy change step is framed in red.

centers. As depicted in Fig. S19,† the release of one –C≡C-CH_3 results in exposure of four shell–metal atoms to form two (111)-like triangular faces. Due to the highly symmetrical structures of $[Ag_9Cu_6(C≡C-CH_3)_{12}]^+$ and $[Au_2Ag_8Cu_5(C≡C-CH_3)_{12}]^+$, the removal of either –C≡C-CH_3 ligand is equivalent. However, it is predicted that, the removal of alkynyl ligand bonded to two Ag atoms near the shell Au atom on the $[Au_2Ag_8Cu_5(C≡C-CH_3)_{12}]^+$ cluster is more thermodynamically supported (the red circle marked in Fig. S19c†), thereby exposing 111-like surfaces (Fig. S19d†). In this context, the H* would readily adsorb to the hollow position of the triangle in a bridging manner (Fig. S20†). The calculated Bader charge (Fig. S20†) shows that the adsorbed *H has a negative charge of -0.11 to -0.22 |e|, suggesting that the adsorbed *H functions as a hydride and may provide the hydrogen source for CO_2 reduction.[24,47] As a consequence, there are four possible reaction channels: (1) proton mechanism of reacting CO_2 with the proton from solution; (2) hydride mechanism of reacting CO_2 with the capping hydride (H*); (3) the hydride–proton or (4) proton–hydride mechanism, where hydride and proton alternately participate in the catalytic process. The free energy difference (ΔG) of each reduction step can be found in Fig. S21 to S23.† On the ligand-removed NCs the proton-reduction channel is preferred for CO; whereas the hydride–proton channel is more favoured for formate, that is, the first adsorbed H* (marked in green) is easily transferred to the C atom to form HCOO*, the second adsorbed H*(marked in blue) is difficult to transfer, but can occupy the active site to facilitate subsequent protonation. The overall mechanism of CO formation via the proton mechanism and formate formation via the hydride–proton mechanism from CO_2 reduction on

three NCs are summarized in Fig. S24 to S26.† The corresponding free energy profile for generating CO and formate are shown in Fig. 5b, d, and f. Apparently, for the CO pathway, the formation of *COOH is the potential-determining step (PDS), the same as on intact NCs; for the formate pathway, the PDS corresponds to the electrochemical protonation of *HCOO to formate or the transfer of H* to the C atom to form HCOO*. Their comparable ΔG for PDS (CO is slightly preferred) indicates that the CO and formate formation is competitive, which is consistent with the experimental observation that CO and formate are the main products on Ag_9Cu_6 and $Au_2Ag_8Cu_5$. The corresponding optimal configurations of key intermediates are depicted in Fig. 6. On both $[Ag_9Cu_6(C{\equiv}C\text{-}CH_3)_{11}]^+$ and $[Au_2Ag_8Cu_5(C{\equiv}C\text{-}CH_3)_{11}]^+$, the two O atoms of HCOO* bind tightly with one Cu atom and one Ag atom on the metal triangle. The active site for CO formation differs from each other, where the *trans*-COOH* prefers to bind to Ag atom on $[Au_7Ag_8(C{\equiv}C\text{-}CH_3)_{11}]^+$, to Cu atom on $[Ag_9Cu_6(C{\equiv}C\text{-}CH_3)_{11}]^+$, and to Au atom on $[Au_2Ag_8Cu_5(C{\equiv}C\text{-}CH_3)_{11}]^+$. The H* on all three clusters easily occupy the hollow sites of the triangle in a bridging manner. Note that, the attraction between the negatively charged H* and the positively charged C of the CO_2 reactant can trigger the favourable H* transfer to form *HCOO, and the participation of metallic Cu as the active center is also important in stabilizing the *HCOO intermediate. Based on the high CO and formate selectivity observed in experiments, the exposure of more active surface metal site upon ligand removal

could be the real reason for the feasible CO_2RR pathway. It is worth noting that we use a simplified $-C{\equiv}C\text{-}CH_3$ group for our simulation, while in experiment, much bulkier butyl groups are employed for protection. To further illustrate the feasibility of this simplification, we investigated the CO_2RR and HER performance of $[Ag_9Cu_6(C{\equiv}C\text{-}^tBu)_{12}]^+$ synthesized in the actual experiment and compared it with $[Ag_9Cu_6(C{\equiv}C\text{-}CH_3)_{12}]^+$. As shown in Fig. S27,† the bulkiness brought by $-C{\equiv}C\text{-}^tBu$ groups slightly weakens the adsorption strength for intermediate state. However, the predicted response and the PDS are basically the same. Thus, the simplification of the butyl ligand can provide valid prediction on the performance.

Discussion on metal core effect of the M_{15} NCs toward CO_2RR

Finally, with the combined experimental and theoretical results of the three M_{15} clusters for CO_2RR, plus the reported Ag_{15} one,[33] we would like to discuss the metal core effect of the M_{15} series toward CO_2RR. Note that, Ag_{15} and Au_7Ag_8 clusters can exclusively convert CO_2 into CO with very high FE values, however, for $Au_2Ag_8Cu_5$ and Ag_9Cu_6 clusters, formate can be generated. Apparently, the presence of Cu atoms is critical for generating formate, and more importantly, with two-atom difference ($Au_2Ag_8Cu_5$ *vs.* Ag_9Cu_6), the catalytic performance is drastically different (the $FE_{formate}$ value for Ag_9Cu_6 is higher than that of $Au_2Ag_8Cu_5$, and the latter one has stronger H_2
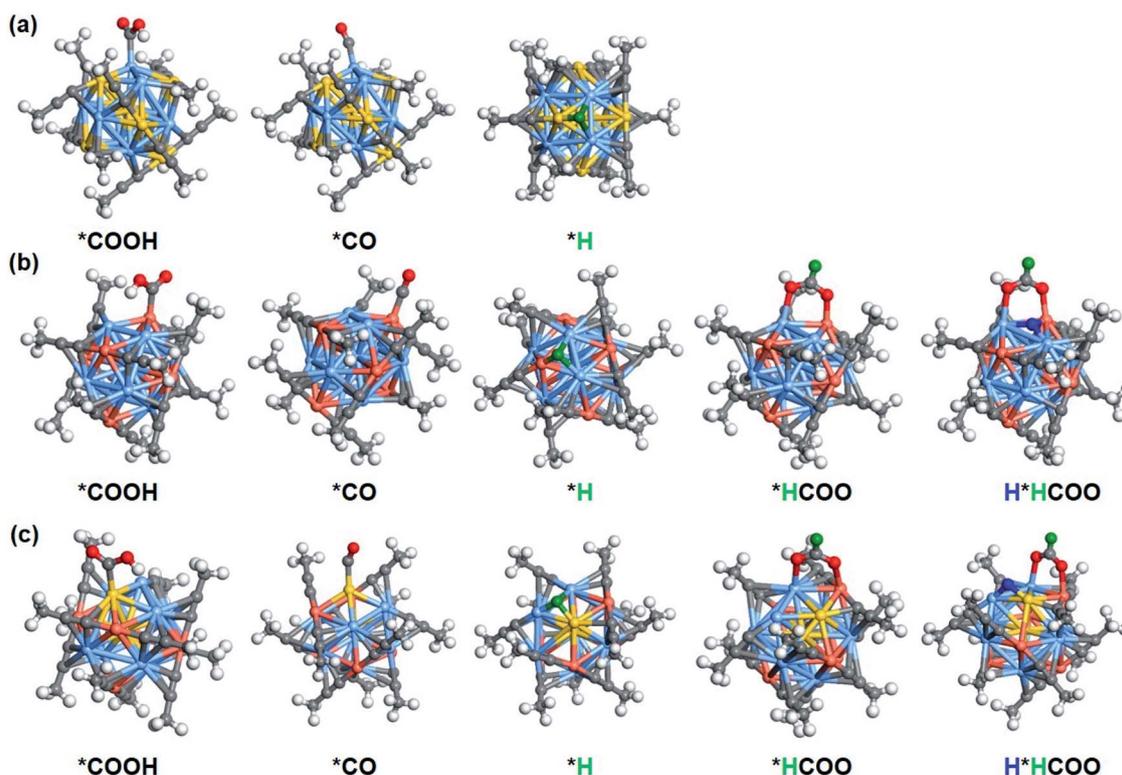

Fig. 6 Schematic presentation of key intermediates on (a) $[Au_7Ag_8(C{\equiv}C\text{-}CH_3)_{11}]^+$, (b) $[Ag_9Cu_6(C{\equiv}C\text{-}CH_3)_{11}]^+$, and (c) $[Au_2Ag_8Cu_5(C{\equiv}C\text{-}CH_3)_{11}]^+$ NCs, respectively. Color legend: Au, gold; Ag, blue; Cu, brick-red; C, gray; O, red; H, white (mark the first H* in green and the second H* in blue).

evolution than formate formation at -1.19 V). That means, strong core size effect toward CO_2RR is observed in the M_{15} series, and metal exchange is an effective strategy to fine-tune the electrocatalytic performance of homoleptic alkynyl-protected metal nanoclusters. The theoretical calculations also support the above findings. For both Ag_{15} and Au_7Ag_8 clusters, the undercoordinated Ag and/or Au atoms upon one intact ligand stripping are the active sites for CO formation. However, for Ag_9Cu_6 and $Au_2Ag_8Cu_5$ NCs, the undercoordinated Cu atoms can serve as the active sites for CO and formate formation. As revealed from Fig. S19,† the different electrocatalytic performance can be ascribed not only from the core atom difference (Ag $vs.$ Au), but more importantly, the exposed (111)-like Ag_2Cu_2 surface and $Au_1Cu_1Ag_2$ surface for Ag_9Cu_6 and $Au_2Ag_8Cu_5$, respectively.

Conclusions

In conclusion, the first all-alkynyl-protected trimetallic superatom of $Au_2Ag_8Cu_5$ is synthesized through a metal exchange approach, of which the formation process is elucidated. $Au_2Ag_8Cu_5$ NC has a similar $M@M_8@M_6$ metal core configuration with Ag_9Cu_6 and Au_7Ag_8 NCs, but quite different absorbance feature. Moreover, the three NCs exhibited drastically different catalytic performance toward CO_2RR, in which Au_7Ag_8 can convert CO_2 into CO exclusively, while CO and formate are the main products for Ag_9Cu_6 and $Au_2Ag_8Cu_5$ at more negative potentials with the highest $FE_{formate}$ of 47.0% and 28.3%, respectively. DFT calculations revealed that ligand stripping can expose more active surface metal atoms to boost CO_2RR activity and selectivity. The formation of surface hydride plays a critical role in triggering the formation and stabilization of HCOO* on the Ag–Cu active center, leading to the exclusive formation of formate in the Cu-containing NCs. Strong core effect toward CO_2RR is observed. This study not only provides an ingenious strategy to tailor the metal core of alkynyl-protected metal NCs at atomic level, but also highlights the unique advantages of employing metal NCs as model catalysts to advance the fundamental mechanistic understanding toward CO_2RR and beyond.

Data availability

All the data in this study are provided in the main text and ESI.†

Author contributions

Z. T. conceived the idea, X. M. conducted most of the experiments, L. Q. and Y. L. helped the characterization, F. S. and Q. T. conducted the DFT calculations, X. K. and L. W. provided the technique support for CO_2RR test, D. J. offered guidance for theoretical calculations, X. M. and Z. T. wrote up the draft, Q. T. and Z. T. provided the funding support, and all the authors contributed to the final proof of the manuscript.

Conflicts of interest

There are no conflicts to declare.

Acknowledgements

Notes and references

1 Q. Lu and F. Jiao, $Nano Energy$, 2016, **29**, 439–456.
2 Y. Wu, Z. Jiang, X. Lu, Y. Liang and H. Wang, $Nature$, 2019, **575**, 639–642.
3 H. B. Yang, S.-F. Hung, S. Liu, K. Yuan, S. Miao, L. Zhang, X. Huang, H.-Y. Wang, W. Cai, R. Chen, J. Gao, X. Yang, W. Chen, Y. Huang, H. M. Chen, C. M. Li, T. Zhang and B. Liu, $Nat. Energy$, 2018, **3**, 140–147.
4 Y. Quan, J. Zhu and G. Zheng, $Small Sci.$, 2021, **1**, 2100043.
5 S. Nitopi, E. Bertheussen, S. B. Scott, X. Liu, A. K. Engstfeld, S. Horch, B. Seger, I. E. L. Stephens, K. Chan, C. Hahn, J. K. Nørskov, T. F. Jaramillo and I. Chorkendorff, $Chem. Rev.$, 2019, **119**, 7610–7672.
6 S. Jin, Z. Hao, K. Zhang, Z. Yan and J. Chen, $Angew. Chem., Int. Ed.$, 2021, **60**, 20627–20648.
7 K. D. Gilroy, A. Ruditskiy, H. C. Peng, D. Qin and Y. Xia, $Chem. Rev.$, 2016, **116**, 10414–10472.
8 S. Zhang, Q. Fan, R. Xia and T. J. Meyer, $Acc. Chem. Res.$, 2020, **53**, 255–264.
9 L. Qin, G. Ma, L. Wang and Z. Tang, $J. Energy Chem.$, 2021, **57**, 359–370.
10 S. Li, A. V. Nagarajan, Y. Li, D. R. Kauffman, G. Mpourmpakis and R. Jin, $Nanoscale$, 2021, **13**, 2333–2337.
11 D. R. Kauffman, D. Alfonso, C. Matranga, H. Qian and R. Jin, $J. Am. Chem. Soc.$, 2012, **134**, 10237–10243.
12 S. Zhao, N. Austin, M. Li, Y. B. Song, S. D. House, S. Bernhard, J. C. Yang, G. Mpourmpakis and R. C. Jin, $ACS Catal.$, 2018, **8**, 4996–5001.
13 B. Kumar, T. Kawawaki, N. Shimizu, Y. Imai, D. Suzuki, S. Hossain, L. V. Nair and Y. Negishi, $Nanoscale$, 2020, **12**, 9969–9979.
14 X. Lin, W. Ma, K. Sun, B. Sun, X. Fu, X. Ren, C. Liu and J. Huang, $J. Phys. Chem. Lett.$, 2020, **12**, 552–557.
15 N. Austin, S. Zhao, J. R. McKone, R. Jin and G. Mpourmpakis, $Catal. Sci. Technol.$, 2018, **8**, 3795–3805.
16 D. R. Alfonso, D. Kauffman and C. Matranga, $J. Chem. Phys.$, 2016, **144**, 184705.

17 S. Li, D. Alfonso, A. V. Nagarajan, S. D. House, J. C. Yang, D. R. Kauffman, G. Mpourmpakis and R. Jin, *ACS Catal.*, 2020, **10**, 12011–12016.

18 S. Zhuang, D. Chen, L. Liao, Y. Zhao, N. Xia, W. Zhang, C. Wang, J. Yang and Z. Wu, *Angew. Chem., Int. Ed.*, 2020, **59**, 3073–3077.

19 S. Li, A. V. Nagarajan, D. R. Alfonso, M. Sun, D. R. Kauffman, G. Mpourmpakis and R. Jin, *Angew. Chem., Int. Ed.*, 2021, **60**, 6351–6356.

20 Y. N. Sun, X. Liu, K. Xiao, Y. Zhu and M. Y. Chen, *ACS Catal.*, 2021, **11**, 11551–11560.

21 Z. X. Tao, Z. S. Wu, Y. S. Wu and H. L. Wang, *ACS Catal.*, 2020, **10**, 9271–9275.

22 Z. Gu, H. Shen, Z. Chen, Y. Yang, C. Yang, Y. Ji, Y. Wang, C. Zhu, J. Liu, J. Li, T.-K. Sham, X. Xu and G. Zheng, *Joule*, 2021, **5**, 429–440.

23 Y. F. Wang, Z. Chen, P. Han, Y. H. Du, Z. X. Gu, X. Xu and G. F. Zheng, *ACS Catal.*, 2018, **8**, 7113–7119.

24 Q. Tang, Y. Lee, D. Y. Li, W. Choi, C. W. Liu, D. Lee and D. E. Jiang, *J. Am. Chem. Soc.*, 2017, **139**, 9728–9736.

25 Z. Lei, X. K. Wan, S. F. Yuan, Z. J. Guan and Q. M. Wang, *Acc. Chem. Res.*, 2018, **51**, 2465–2474.

26 Z. Lei and Q.-M. Wang, *Coord. Chem. Rev.*, 2019, **378**, 382–394.

27 P. Maity, S. Takano, S. Yamazoe, T. Wakabayashi and T. Tsukuda, *J. Am. Chem. Soc.*, 2013, **135**, 9450–9457.

28 X. Ma, Y. Tang, G. Ma, L. Qin and Z. Tang, *Nanoscale*, 2021, **13**, 602–614.

29 Z. Lei, X. K. Wan, S. F. Yuan, J. Q. Wang and Q. M. Wang, *Dalton Trans.*, 2017, **46**, 3427–3434.

30 P. Yuan, R. Zhang, E. Selenius, P. Ruan, Y. Yao, Y. Zhou, S. Malola, H. Hakkinen, B. K. Teo, Y. Cao and N. Zheng, *Nat. Commun.*, 2020, **11**, 2229.

31 Z. Y. Wang, M. Q. Wang, Y. L. Li, P. Luo, T. T. Jia, R. W. Huang, S. Q. Zang and T. C. W. Mak, *J. Am. Chem. Soc.*, 2018, **140**, 1069–1076.

32 T. T. Jia, G. Yang, S. J. Mo, Z. Y. Wang, B. J. Li, W. Ma, Y. X. Guo, X. Chen, X. Zhao, J. Q. Liu and S. Q. Zang, *ACS Nano*, 2019, **13**, 8320–8328.

33 L. Qin, F. Sun, X. Ma, G. Ma, Y. Tang, L. Wang, Q. Tang, R. Jin and Z. Tang, *Angew. Chem., Int. Ed.*, 2021, **60**, 26136–26141.

34 X. Ma, L. Xiong, L. Qin, Y. Tang, G. Ma, Y. Pei and Z. Tang, *Chem. Sci.*, 2021, **12**, 12819–12826.

35 X. Kang, X. Wei, X. Liu, S. Wang, T. Yao, S. Wang and M. Zhu, *Nat. Commun.*, 2021, **12**, 6186.

36 H. Shen, Z. Xu, L. Wang, Y. Z. Han, X. Liu, S. Malola, B. K. Teo, H. Hakkinen and N. Zheng, *Angew. Chem., Int. Ed.*, 2021, **60**, 22411–22416.

37 Y. Wang, H. Su, L. Ren, S. Malola, S. Lin, B. K. Teo, H. Hakkinen and N. Zheng, *Angew. Chem., Int. Ed.*, 2016, **55**, 15152–15156.

38 Z. Tang, D. A. Robinson, N. Bokossa, B. Xu, S. Wang and G. Wang, *J. Am. Chem. Soc.*, 2011, **133**, 16037–16044.

39 W. Du, S. Jin, L. Xiong, M. Chen, J. Zhang, X. Zou, Y. Pei, S. Wang and M. Zhu, *J. Am. Chem. Soc.*, 2017, **139**, 1618–1624.

40 X. Zou, Y. Li, S. Jin, X. Kang, X. Wei, S. Wang, X. Meng and M. Zhu, *J. Phys. Chem. Lett.*, 2020, **11**, 2272–2276.

41 T. Higaki, Q. Li, M. Zhou, S. Zhao, Y. Li, S. Li and R. Jin, *Acc. Chem. Res.*, 2018, **51**, 2764–2773.

42 Q. Li, T. Y. Luo, M. G. Taylor, S. Wang, X. Zhu, Y. Song, G. Mpourmpakis, N. L. Rosi and R. Jin, *Sci. Adv.*, 2017, **3**, e1603193.

43 A. Ghosh, O. F. Mohammed and O. M. Bakr, *Acc. Chem. Res.*, 2018, **51**, 3094–3103.

44 X. Kang, X. Wei, S. Jin, Q. Yuan, X. Luan, Y. Pei, S. Wang, M. Zhu and R. Jin, *Proc. Natl. Acad. Sci.*, 2019, **116**, 18834–18840.

45 K. Zheng, V. Fung, X. Yuan, D. E. Jiang and J. Xie, *J. Am. Chem. Soc.*, 2019, **141**, 18977–18983.

46 H. Seong, V. Efremov, G. Park, H. Kim, J. S. Yoo and D. Lee, *Angew. Chem., Int. Ed.*, 2021, **60**, 14563–14570.

47 F. Li and Q. Tang, *J. Catal.*, 2020, **387**, 95–101.